

Journal of Materials Chemistry A

Accepted Manuscript



This is an *Accepted Manuscript*, which has been through the Royal Society of Chemistry peer review process and has been accepted for publication.

Accepted Manuscripts are published online shortly after acceptance, before technical editing, formatting and proof reading. Using this free service, authors can make their results available to the community, in citable form, before we publish the edited article. We will replace this *Accepted Manuscript* with the edited and formatted *Advance Article* as soon as it is available.

You can find more information about *Accepted Manuscripts* in the [Information for Authors](#).

Please note that technical editing may introduce minor changes to the text and/or graphics, which may alter content. The journal's standard [Terms & Conditions](#) and the [Ethical guidelines](#) still apply. In no event shall the Royal Society of Chemistry be held responsible for any errors or omissions in this *Accepted Manuscript* or any consequences arising from the use of any information it contains.



Role of Nanoscale-range Vanadium Treatment on $\text{LiNi}_{0.8}\text{Co}_{0.15}\text{Al}_{0.05}\text{O}_2$ Cathode Materials for Li-ion Batteries at Elevated Temperatures†

Cite this: DOI: 10.1039/x0xx00000x

Received 00th January 2012,
Accepted 00th January 2012

DOI: 10.1039/x0xx00000x

www.rsc.org/MaterialsA

Min-Joon Lee,‡ Mijung Noh,‡ Mi-Hee Park, Minki Jo, Hyejung Kim, Haisol Nam and Jaephil Cho*

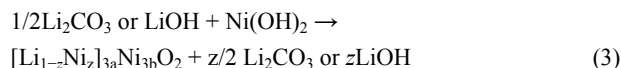
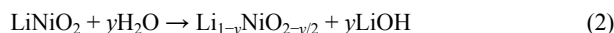
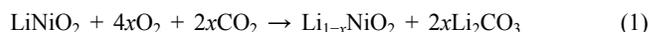
In order to overcome the inherent structural instability of bare $\text{Li}_x\text{Ni}_{0.8}\text{Co}_{0.15}\text{Al}_{0.05}\text{O}_2$ (BNCA) containing large amounts of LiOH and Li_2CO_3 impurities at 60 and $>200^\circ\text{C}$, an effective nanoscale layer was generated by coating BNCA with an ammonium vanadate precursor, followed by annealing at 400°C . This process forms a 17nm-thick surface layer containing V^{4+} ions into the transition metal 3b sites, thereby decreasing the thickness of the cation-mixing layer, which is the main factor responsible for destabilizing the surface structure. Such a coating also helps in substantially reducing the amount of surface impurities of LiOH, Li_2CO_3 , and H_2O by forming LiVO_2 , LiV_2O_5 , VO_2 , and V_2O_5 . Consequently, at 60°C , vanadium-treated $\text{LiNi}_{0.8}\text{Co}_{0.15}\text{Al}_{0.05}\text{O}_2$ (VNCA) demonstrated excellent cycleability with a discharge capacity of 179 mAh g^{-1} after 200 cycles (after 17 days) between 3 and 4.3 V, corresponding to 90% capacity retention, which is 18% higher than the capacity retention measured for BNCA. More importantly, VNCA exhibits a significantly reduced heat generation and a higher onset temperature for exothermic reactions.

Introduction

The increasing demand of high-energy storage devices for fully electrical vehicles (EVs) and portable electronics have led to the development of batteries with high energy densities.^{1, 2} Layered materials such as LiMO_2 (M = Ni, Co, Mn, Al, etc.) have been extensively investigated as potential candidates for cathodes. In particular, Ni-rich $\text{Li}_z\text{Ni}_{1-x}\text{M}_x\text{O}_2$ ($1-x > 0.6$; M = Co, Mn, Al, etc.) materials are considered to be the most promising candidates because of their high specific capacity (above 190 mAh g^{-1}).^{3, 4} However, on increasing the nickel content, higher concentrations of unstable Ni^{4+} ions easily migrate from the transition metal layer to the lithium layer; This migration generates Ni^{2+} ions in the lithium layer (cation-mixing layer or rock salt NiO phase) on the cathode surface, increasing the interfacial resistance, which in turn reduces the rate capability of the overall system.⁵⁻⁹ The ion migration tends to initiate at the structurally weakened surface of the particles and to propagate into their core. Accordingly, the $\text{LiNi}_{0.8}\text{Co}_{0.15}\text{Al}_{0.05}\text{O}_2$ material shows poor cycle retention, especially at 60°C , and results in violent exothermic reactions with the electrolytes above 200°C . In addition, this material exhibits a higher absorption of CO_2 than $\text{LiNi}_{1/3}\text{Co}_{1/3}\text{Mn}_{1/3}\text{O}_2$.¹⁰

In order to improve the electrochemical properties and thermal stability of the cathode, surface treatments such as coating and doping have been proposed,¹¹⁻¹⁸ together with the use of core-shell materials^{19, 20}. Generally, surface-coating materials such as metal oxides, fluorides, and phosphates are used to protect the surface from hydrofluoric acid (HF) attack and other side reactions between the cathode materials and the electrolyte.²¹ However, such insulating coating layers, which have a low ionic and a low electronic conductivity, tend to increase the surface resistance.²²

Another critical problem of Ni-rich cathodes is the presence of lithium impurities (such as LiOH and Li_2CO_3) on their surface because of the exposure to CO_2 and moisture in air or use of excessive amounts of lithium sources during the preparation phase. The formation of such impurities is always accompanied by the generation of cation-mixing phase according to the following reactions:²³⁻²⁵



For the cathode powder, reducing the amounts of residual LiOH, H_2O , and Li_2CO_3 impurities are very important because they hinder Li^+ diffusion and charge-transfer reactions at the interface and they accelerate the formation of HF.^{21, 26} Furthermore, Li_2CO_3 has been

School of Energy and Chemical Engineering, Ulsan National Institute of Science and Technology (UNIST), Ulsan, 689-798, South Korea.

E-mail: jpcho@unist.ac.kr

† Electronic Supplementary Information (ESI) available: Table S1, and Figure S1–S5. See DOI: 10.1039/b000000x/

‡ These authors equally contributed to this work.

reported to be the main source of CO₂ evolution during the electrochemical process at 60 °C. Finally, the pH of the cathode powder in water should be maintained below 12, otherwise the cathode composite slurry, which is prepared by using *N*-methyl-2-pyrrolidone (NMP) as a solvent, exhibits a rapid increase in its viscosity, eventually resulting in gelation.²⁷

Even though the surface coating technique is well-known and common practice to improve performances of electrode materials, lower temperature coating methods that induces the surface structure fortification of the Ni-rich cathodes (LiNi_{1-x}M_xO₂, 1-x ≥ 0.8) have not been explored. For instance, in spite of the importance of LiNi_{0.8}Co_{0.15}Al_{0.05}O₂ as a cathode material (it is the best candidate for EV batteries), sole use of this cathode in the Li-ion batteries is hindered by poor cycling performance at 60 °C and thermal instability above 200 °C. Washing and annealing process at < 200 °C may reduce the lithium impurities on the cathode surface, but prolonged cycling instability at 60 °C and thermal instability above 200 °C cannot be solved. Some previous studies have been proposed on optimizing the LiNi_{0.8}Co_{0.15}Al_{0.05}O₂ material in order to make them suitable for use at 60 °C and to enhance their thermal stability above 200 °C (Table S1).²⁸⁻³⁴

Recently, V₂O₅ or VO_x coatings on cathode materials were reported not only to improve the electrochemical performance because of the reduced amount of lithium impurities, but also to moderate the dissolution of transition metals.³⁵⁻³⁸ For instance, Xiong et al. reported that the V₂O₅ coating could reduce the amount of residual lithium impurities in LiNiO₂.^{39, 40} However, there are no literatures to provide the specific information about the compound of vanadium on the surface and the structural changes of layered materials after coating as well as cycling at 60 °C and thermal stability.

In this regard, we reported a novel LiNi_{0.8}Co_{0.15}Al_{0.05}O₂ cathode material featuring V⁴⁺ ions in the 3b sites with a superficial layer. The coating layer synthesized via the simple sol-gel method, which is economically beneficial, acts as the protecting layer against the HF attack. The layer provided the structural stability under the most challenging test conditions such as prolonged cycles at 60 °C over 17 days, thermal stability tests above 200 °C, and even intermittent pulse tests at 60 °C.

Experimental

Synthetic Method

To begin, Ni_{0.8}Co_{0.15}Al_{0.05}(OH)₂ powder was synthesized via co-precipitation method.⁴¹ The obtained powder was thoroughly mixed with appropriate amount of LiOH. The mixture was preheated at 500 °C for 5h and subsequently calcined at 800 °C for 10h in furnace under oxygen condition to form LiNi_{0.8}Co_{0.15}Al_{0.05}O₂. In order to prepare the coated VNCA cathode, 0.307 g of NH₄VO₃ (ammonium metavanadate) was dissolved in ethanol for an hour at 65 °C, and 100 g of BNCA powder was added and thoroughly mixed as the temperature of hotplate increased slowly to 110 °C for an hour. The mixture was mixed vigorously with BNCA at 110 °C until ethanol removal. The result powders were heated at 400 °C for 3 hours.

Characterizations

X-ray photoelectron spectroscopy (XPS) analyses were performed with a Thermo fisher, K-Alpha spectrometer using a monochromatic Al K α radiation of an energy beam (1486.6 eV). Spectra were recorded in the constant pass energy mode at 200.0 eV using a 100 μ m diameter analysis area. For the depth profile, Ar-ion etching was used for 0-200 s. The crystalline phase was analyzed by powder X-ray diffractometer (XRD, D/MAX-2200 V, Rigaku) using Cu K α radiation at 2 θ = 10 °-80 °. Rietveld refinements of the obtained

materials were calculated by GSAS program. To investigate the phase transition of the samples depending on temperature from 100 to 300 °C at a scan rate of 5 °C min⁻¹, powder XRD (D/MAZX 2500V/PC) measurements using CuK α radiation were used. The morphology of prepared powders was examined using scanning electron microscopy (SEM, S-4800, HITACHI). Transmission electron microscopy sample was prepared by focused ion beam (FIB, Quanta 3D FEG, FEI). The high resolution transmission electron microscopy (HR-TEM, EDS, EELS, JEM-2100F, JEOL) operating at 200 kV was used for analyzing a microstructure with an atomic scale. Time-of-flight (TOF) Secondary ion mass spectrometry (SIMS) analysis was carried out in the TOF-SIMS 5 instrument. The data in this study were obtained in Chemical mapping and Trace elemental analysis mode. TOF-SIMS surface analyzer operated at 10-9 Torr using a liquid Ga ion source. For the analysis, the targets were bombarded by 15 keV Ga beams, with the pulsed primary ion current varying from 0.3 to 0.5 pA. Two dimensional ion mapping of the electrode was obtained by bombarding using 2Bi³⁺ cluster ions. DSC data of the electrodes were collected as follows. The cells were charged to 4.3 V at a rate of 0.1 C (1C = 210 mA g⁻¹), and then the charged cells were disassembled in a dry room to collect the electrodes. The dissembled electrodes were washed with DMC solvent and dried in a dry room. The dried sample and 30 wt% electrolyte were hermetically sealed inside stainless steel high-pressure capsules to prevent leakage of the pressurized solvents. The DSC curves were measured between room temperature to 350 °C at a scan rate of 5 °C min⁻¹. The measurements of pH were carried out as follows. The 5 g of powders was immersed into 50 g of water and then, the pH of mixtures was measured every 1 min during continuous stirring.

Electrochemical characterizations

The cathode electrode is composed of cathode material, Super P as a conductive additive, and poly (vinylidene fluoride) (PVdF) as a binder (92:4:4 weight ratio). Coin-type lithium cells (2032R) were assembled in an argon-filled glove box using lithium metal as a counter electrode, micro porous polyethylene as a separator, and 1.15 M LiPF₆ in ethylene carbonate/dimethyl carbonate/diethyl carbonate (3/4/3 vol.%; Panax Starlyte) as the electrolyte. All electrochemical tests were performed on WBCS-3000 (WonATech Co.). The galvanostatic charge-discharge tests were conducted in a voltage range of 4.3 to 3.0 V vs. Li/Li⁺. The active material loading was 7 mg cm⁻², and the electrode density was 3.0 g cm⁻³, respectively. Electrochemical impedance spectroscopy (EIS) was performed from 0.05 to 250 kHz frequency range using electrochemical interface system (IVIUM) on coin-type half cells at SOC 80% (4.1 V). All the fittings were carried out with Solatron software "Zview".

Results and discussion

Figure 1a shows a schematic view of the coating process. First, the NH₄VO₃ powder was dissolved in ethanol, and then the cathode powder was added to the solution. The solution was vigorously mixed with a homogenizer and was heated at 110 °C on hotplate; NH₄VO₃ was ionized to VO₃⁻, which reacted with Li⁺ ions originating from the dissolved lithium impurities. The resulting dried powder was baked at 400 °C for 3 h. We could not apply coatings that require annealing temperatures above 600 °C because of the risk of the collapse of the round-type pristine morphology (Figure S1). In spite of this low

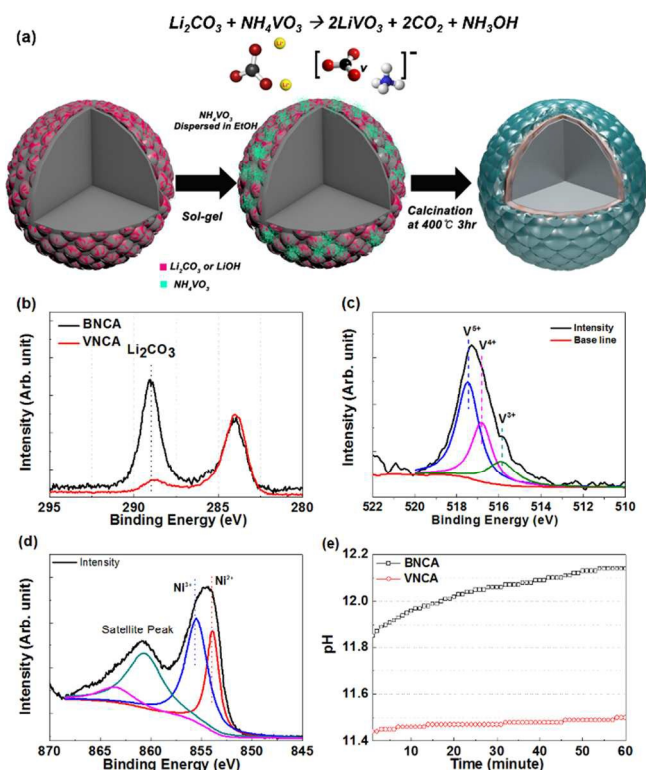


Figure 1. (a) Schematic view of the coating process of BNCA performed using NH_3VO_3 ; XPS spectra of VNCA; (b) carbon (the peak at 284.4 eV draws a distinction between the standard carbon and the carbon background), (c) vanadium, and (d) nickel. (e) Plot of pH vs. measuring time in a mixture of BNCA or VNCA powders and water.

temperature coating method, the VNCA demonstrated significantly improved electrochemical performances at elevated temperatures as described below. The Karl-Fisher titration method in the mixed solution of HCl was used to estimate the total amount of lithium impurities in BNCA, namely 0.16 wt%. However, because the Li_2VO_5 oxides formed on the particle surface easily dissolve in such an acidic solution, a different methodology was used. The X-ray photoelectron spectroscopy (XPS) profile for C1s on the surface of both the electrode samples shows that the carbon peak of Li_2CO_3 at 289.5 eV almost disappeared after the coating process (Figure 1b). This result indicates that the residual lithium impurities on the cathode surface were effectively removed.

Figures 1c and d display the XPS spectra of $\text{V}2\text{p}_{3/2}$ and $\text{Ni}2\text{p}_{3/2}$ in outmost surface of VNCA, respectively. The deconvoluted peaks of the $\text{V}2\text{p}_{3/2}$ spectrum at 517.5, 516.5, and 515.5 eV indicate the formation of $\text{V}^{\text{m}+}$ ions, where $m = 5+$ (V_2O_5), $4+$ (LiV_2O_5 , VO_2) and $3+$ (LiVO_2) ions and V^{5+} (V_2O_5) is the dominant species among them. The deconvoluted peak of the $\text{Ni}2\text{p}_{3/2}$ spectrum at 853.9 eV shows a lower $\text{Ni}^{3+}/\text{Ni}^{2+}$ peak intensity ratio than that for BNCA (Figure S2). This finding indicates that Ni^{2+} ions were formed at the expense of Ni^{3+} ions to compensate for the presence of V^{4+} ions in the 3b sites, according to the following equation:

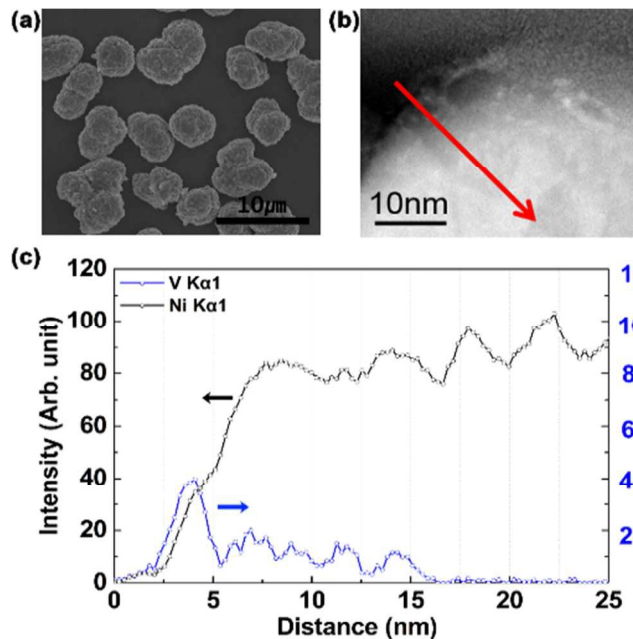
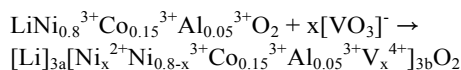


Figure 2. (a) SEM and (b) TEM images of the cross section of a VNCA sample. (c) EDX distribution of V and Ni elements along the red arrow shown in (b).

The pH of the BNCA and VNCA powders was estimated in water; the initial pH values were 11.85 and 11.44 for BNCA and VNCA, respectively, but the pH value of the BNCA powder rapidly increased to 12.14 after 60 min, whereas that of the VNCA powder stopped at 11.50 (Figure 1e). The reason of such increase in the pH value is related to the dissolution of Li_2CO_3 and LiOH , and, possibly, to the Li^+ ion loss from the cathodes.⁴² In general, a pH value above 12 in the cathodes rapidly increased the slurry viscosity during the mixing process in NMP; therefore, it is recommended to maintain the pH value below 12.

An energy dispersive X-ray (EDX) line scanning of Ni and V was carried out along the red arrow shown in the cross section of the VNCA sample, which was obtained using a focused ion beam (FIB). The findings show that Ni and V coexist in a ~17 nm thick superficial layer (Figure 2b and c). No coating layer comprising by-products such as LiV_2O_5 , VO_2 , and V_2O_5 was observed. This suggests that the by-products may be distributed locally, throughout the particles, or that the by-products layer may be too thin to be detected. In order to confirm the coating layer and its compositions, a time of flight secondary ion micro spectroscopy (TOF-SIMS) analysis was conducted on VNCA (0.4 mol% NH_4VO_3). The findings show that the surface mainly consisted of LiVO_2 , LiV_2O_5 , VO_2 , and V_2O_5 (Figure 3). However, when the NH_4VO_3 content in the coating was increased to 0.8 mol%, the VO_2 and V_2O_5 content appeared to increase, whereas the LiV_2O_5 content remained constant, indicating that 0.4 mol% of NH_4VO_3 in the coating is sufficient to remove lithium impurities. Consequently, based on the above the results, it is reasonable to infer that some portion of vanadium ions are doped to transition metal sites and the rest of ions react with lithium impurities resulting in the formation of lithium vanadium oxide compounds on the surface of BNCA as the coating materials.

Figure 4a and b show the scanning transmission electron microscopy (STEM) images of BNCA and VNCA and their

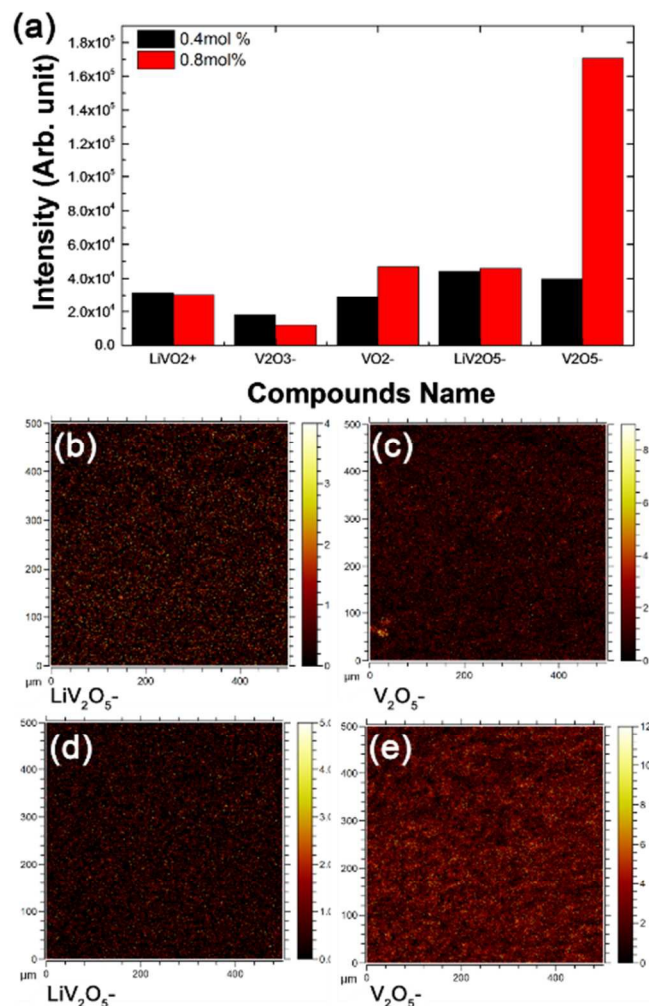


Figure 1. Intensity of Li₂VO_y species obtained from TOF-SIMS in the VNCA electrode obtained by using two different coating contents, 0.4 and 0.8 mol% of NH₃VO₃. TOF-SIMS mapping images of LiV₂O₅⁻ and V₂O₅⁻ in the VNCA electrodes with 0.4 mol% (b, c) and 0.8 mol% (d, e) NH₃VO₃.

high-magnification images are shown in Figure 4c and d along the [100]_{trigonal} zone axis. The high-angle annular dark-field (HAADF) STEM images have been frequently used to analyse the crystalline structures and defects such as cation-mixing and oxygen deficiency with an atomic scale.⁴³⁻⁴⁶ In the HAADF images, the transition metal columns appeared as white dots, while the lithium columns were indiscernible because lithium is a light element. The BNCA sample clearly shows the cation-mixing layer extending inward for ~15 nm from the surface, whereas the cation-mixing layer is only ~2 nm for the VNCA sample. These results agree with the Rietveld analysis performed in the samples, showing a decreased degree of cation-mixing in VNCA (Table S2 and Figure S3)

In order to test the applicability of the cathode materials in the Li-ion cells, the cathode electrode was tested for a loading level of active material of 7 mg cm⁻² and a content of active material, binder and conductive material of 92, 4, and 4 wt%, respectively. The first discharge capacities of BNCA and VNCA were 198 and 199 mAh g⁻¹, respectively, when tested between 3.0 and 4.3 V, at 0.1 C rate (21 mA g⁻¹) and 24 °C (Figure S4). The higher capacity of VNCA is due to the increased Coulombic efficiency (94% instead of 93%)

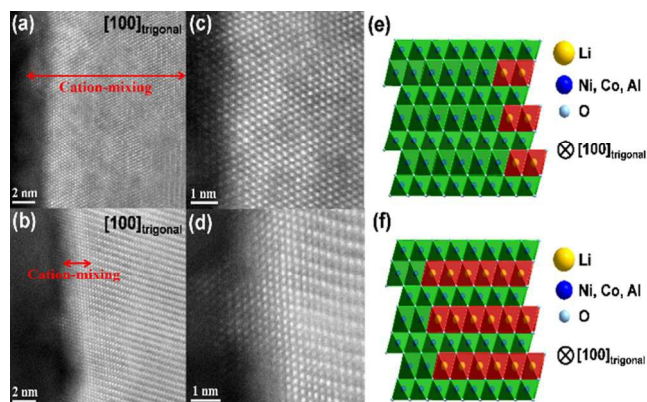


Figure 4. HAADF STEM images of bulk surfaces of (a) BNCA and (b) VNCA. (c,d) Magnified images of (a,b), respectively. (e,f) Structural schematic diagrams of BNCA and VNCA, respectively.

compared to BNCA. This is possibly due to the effective removal of lithium impurities on the cathode material. One of the critical tests for the Ni-rich cathode material is the cycling stability at 60 °C, because at this temperature the structural degradation associated with the metal dissolution is accelerated by the side reactions involving the electrolytes. Figure 5a displays the cycling performances of BNCA and VNCA during 200 cycles at 60 °C between 3.0 and 4.3 V at 1 C rate and their voltage profiles are shown in Figure S5. The discharge capacity retention of the VNCA sample after 200 cycles at the 1 C rate was 90%, corresponding to 179 mAh g⁻¹, whereas the BNCA sample showed a discharge capacity retention of only 78%. As far as we know, such capacity retention value (90%) at 60 °C has not been reported before. The retention of the working voltage (defined as the voltage corresponding to the middle value of the capacity) also showed a meaningful result (Figure 5b), and the VNCA sample showed a constant voltage retention, in contrast to the BNCA sample, up to 200 cycles, providing higher energy than the BNCA sample. Figure 5c shows the discharge capacity variation of BNCA and VNCA after being stored for 10 h and 1 week in the charged state at 4.3 V and 60 °C. The VNCA sample showed a much improved capacity retention compared to the BNCA sample, which is ascribable to the suppression of the transition metal dissolution, usually due to the HF attack on the cathode surface.^{47, 48} Since the intermittent high rate discharge is also a critical condition for EVs, pulse rate measurements of the BNCA and VNCA cathodes were carried out in a lithium half-cell at 60 °C (Figure 5d).⁴⁹ Every 20 cycles, a 5 C discharge current was applied for 1 cycle, maintaining the charge rate at 0.5 C over 100 cycles (Figure S6). Notably, the sudden capacity drop upon pulse cycle was larger for the BNCA sample than for the VNCA sample. The VNCA sample maintained a 10 mAh g⁻¹ capacity drop throughout the pulse test, whereas the capacity drop for the BNCA sample kept increasing from 80 to 120 mAh g⁻¹. Also the rate capability of VNCA was much higher than that of BNCA, especially at higher C-rate (Figure 5e). For example, the discharge capacity retention of VNCA electrode at 10 C was 67.8% (127 mAh g⁻¹) of its discharge capacity at 0.2 C, while that of the BNCA electrode delivered only 36.1% (67 mAh g⁻¹). It is believed that these improved stabilities such as cycling and storage performances were mainly associated with the decreased lithium impurities and the stable surface leading to the lower charge-transfer resistance during the electrochemical cycling. As can be seen in Figure S7 and Table

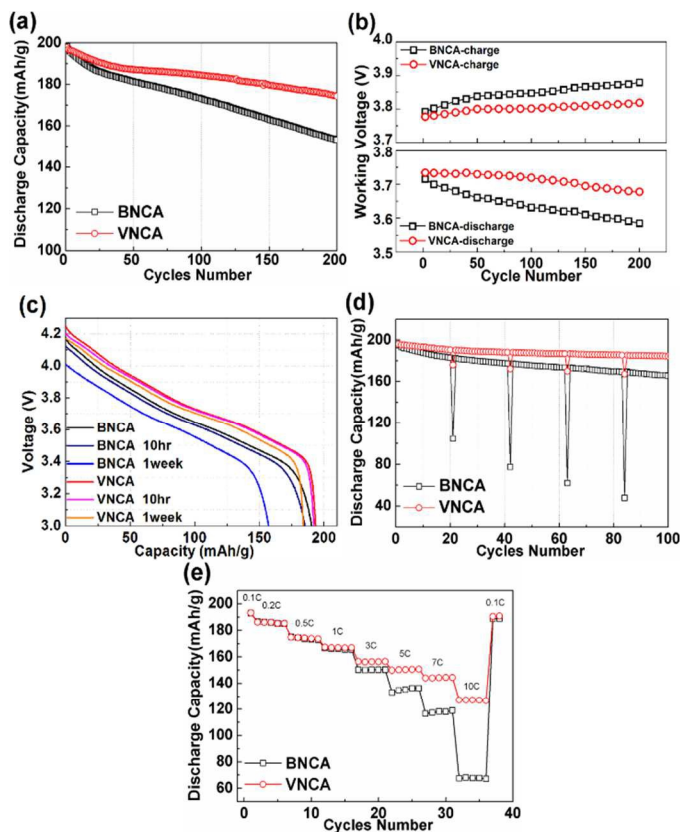


Figure 5. (a) Cycling performances of BNCA and VNCA cathodes in lithium half-cells (2032R) during 200 cycles at 1 C rate (equivalent to 210 mA g^{-1}) at 60°C . (b) Plot of working voltage vs. cycle number for BNCA and VNCA cathodes. (c) Discharge curves of BNCA and VNCA cathodes under 1 C rate discharge after being stored at 4.3 V for 10 h and 1 week at 60°C . (d) Plot of discharge capacity vs. cycle number in the BNCA and VNCA cathodes at 60°C . A pulse corresponding to 5 C rate was applied every 20 cycles. (e) Rate capabilities of BNCA and VNCA cathodes under same charge and discharge c-rate for 0.1 C and 0.2 C, and 0.5 C charge c-rate for higher than or equal to 0.5 C discharge c-rate at 24°C .

S3, the $R_f + R_{ct}$ of BNCA appeared to greatly increase on increasing the number of cycles, in contrast to the $R_f + R_{ct}$ of VNCA at 60°C . The TOF-SIMS analysis of both the samples after cycling indicated the formation of impurities such as LiF, Li_2O , Li_2CO_3 , NiO, and MF_x ($M = \text{Ni, Co}$) on the surface (Figure S8); however, their intensity ratios were much smaller for VNCA than for BNCA, indicating that the V^{4+} ion-substituted bulk surface layer effectively suppresses the side reactions with the electrolyte and minimizes metal dissolution. In other words, the $\sim 17 \text{ nm}$ thick bulk surface layer was structurally hardened by V^{4+} ion substitution. Combined with the results of TOF-SIMS analysis, these findings indicate that the impurities and unstable surface caused the increase of the charge-transfer resistance in the cathode and electrolyte interface. The improved rate capability was associated with the higher lithium ion diffusivities (D_{Li^+}) as well as the reduced charge-transfer and surface film resistances (Figure S7). The D_{Li^+} was determined by Warburg impedance in the low frequency region.⁴⁴ The D_{Li^+} of BNCA is $6.97 \times 10^{-11} \text{ cm}^2 \text{ S}^{-1}$, while that of VNCA is $9.16 \times 10^{-11} \text{ cm}^2 \text{ S}^{-1}$. It is believed that

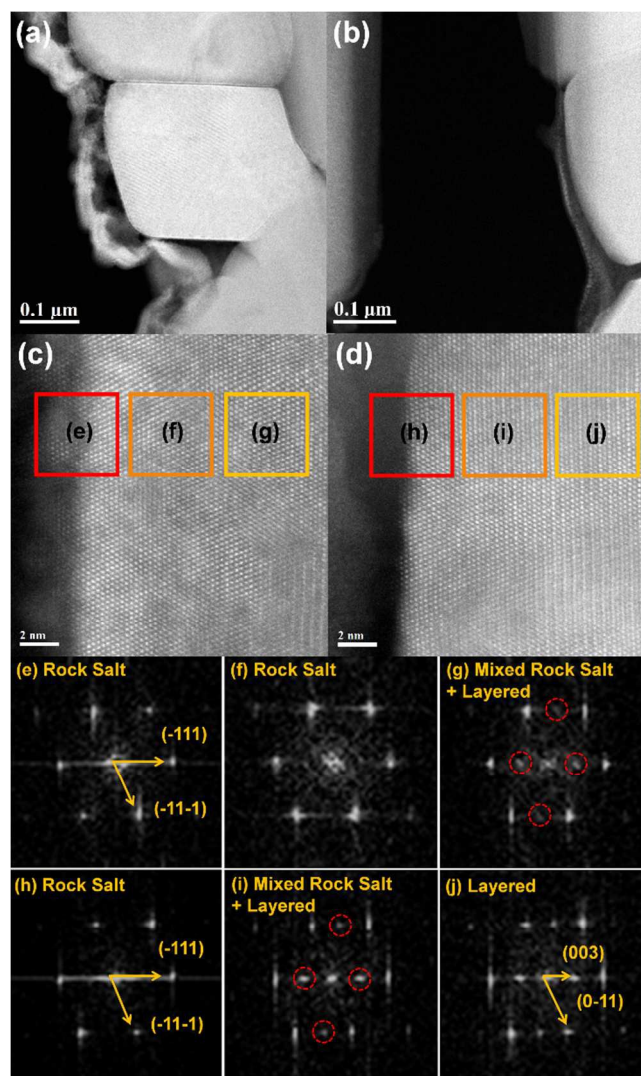


Figure 6. STEM images of (a) BNCA and (b) VNCA after 200 cycles at 60°C ; (c) and (d) are expanded images of (a) and (b), respectively. Fast Fourier transform images of (e-g) BNCA and (h-j) VNCA

the increased diffusivity is ascribable to the reduced thickness of cation-mixing phase, which leads to the facile lithium ion diffusion. Consequently, the rate capability was enhanced after the vanadium treatment.

The TEM images of the cross sectioned samples after 200 cycles at 60°C showed the presence of white impurity layers along the primary particles (Figure 6a and b). These layers are in agreement with the lithium and transition metal compounds (Figure S8). As can be seen, the layers on the VNCA sample are thinner than those on the BNCA sample (Figure 6a and b). This correlates well with the aforementioned results. As shown in Figure 6c, the surface region of the BNCA sample ($> 10 \text{ nm}$) mostly consists of the rock salt NiO phase with space group $Fm-3m$ (Figure 6e-g) and the dots with weak contrast demonstrate the small amount of layered phases is mixed with the rock salt phase in that region (Figure 6g). The outermost region of VNCA shows the rock salt phase like that of BNCA (Figure 6h), while the inner regions mostly consists of layered phase (Figure 6i and j). These result indicates that the structural

stability of the VNCA is higher than that of the BNCA, which resulted in the improved electrochemical performances.

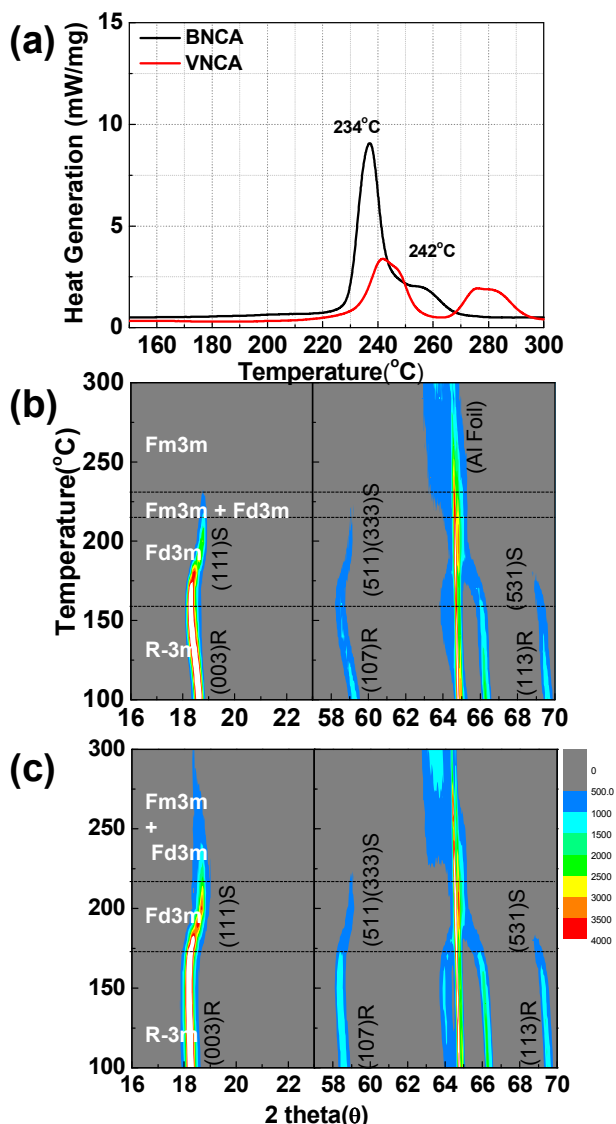


Figure 7. (a) Differential scanning calorimetry of BNCA and VNCA charged at 4.3 V and (b) contour plots of in situ HT-XRD of (b) BNCA and (c) VNCA after charging at 4.3 V.

The thermal instability of the cathode material during delithiation is an important concern for commercialization and it is directly related to phase transition due to oxygen evolution from the lattice. The thermal characteristics of the cathode materials were evaluated by high temperature X-ray diffractometer (HT-XRD) and differential scanning calorimetry (DSC) analyses after the samples were charged to 4.3 V (Figure 7), with the latter being a powerful technique for investigating the structure stability. The total amount of heat generated for the VNCA sample from 50 to 300 °C was estimated to be 803 J g⁻¹, a significantly lower value than the one measured for the BNCA sample, 1450 J g⁻¹ (Figure 7a). Such heat generation is a result of continuous structural changes due to oxygen losses from their lattices. This result agrees well with the HR-XRD findings (Figure 7b and c). The initial XRD patterns of the BNCA and VNCA samples at 100 °C show (003), (107), and

(113) peaks, indicating rhombohedral phase formation (*R-3m*). However, this phase transformed into a disordered spinel (*Fd-3m*), beginning at ~155 °C, then into rock salt (*Fd-3m*) phase at ~215 °C, and finally into *Fm-3m* at ~230 °C (Figure 7b). The VNCA sample (Figure 7c) showed a different phase transition behavior with a transformation from the *R-3m* phase to the *Fd-3m* phase at ~175 °C, a higher temperature than the one required for the BNCA sample. When the VNCA samples are heated above 220 °C, the *Fd-3m* and *Fm-3m* phases coexist and are present in the sample until 300 °C. It is well known that the host structure undergoes oxygen release from the lattice, when the crystal phase is changed from *R-3m* to *Fd-3m*, and from *Fd-3m* and *Fm-3m*.⁵⁰ The vanadium treatment is quite effective in delaying phase transitions, which leads to the deferred oxygen evolution and reducing the amount of released oxygen. Consequently, the exothermic peaks shifted to the higher temperature and the generation heat was greatly reduced.

Conclusions

The bulk surface protecting effect of LiNi_{0.8}Co_{0.15}Al_{0.05}O₂ on the electrochemical performance at elevated temperatures achieved by V-based coating was investigated with the help of various electrochemical tests. The VNCA cathode material demonstrated significantly improved cycling stability under constant voltage and pulse tests at 60 °C because of the reduction in the thickness of the cation-mixing layer and formation of a ~17 nm thick bulk surface layer containing V⁴⁺ ions.

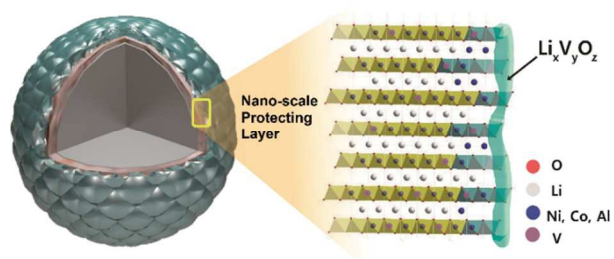
Acknowledgements

This research was supported by MSIP (Ministry of Science, ICT & Future Planning), Korea, under the C-ITRC (Convergence Information Technology Research Center) support program (NIPA-2013-H0301-13-1009) supervised by the NIPA (National IT Industry Promotion Agency).

References

1. V. Etacheri, R. Marom, R. Elazari, G. Salitra and D. Aurbach, *Energy Environ. Sci.*, 2011, 4, 3243-3262.
2. D. P. Abraham, E. M. Reynolds, E. Sammann, A. N. Jansen and D. W. Dees, *Electrochim. Acta*, 2005, 51, 502-510.
3. C. Delmas, M. Ménétrier, L. Croguennec, I. Saadoune, A. Rougier, C. Poullierie, G. Prado, M. Grüne and L. Fournès, *Electrochim. Acta*, 1999, 45, 243-253.
4. A. M. Kannan and A. Manthiram, *J. Electrochem. Soc.*, 2003, 150, A349-A353.
5. J. Shim, R. Kostecki, T. Richardson, X. Song and K. A. Striebel, *J. Power Sources*, 2002, 112, 222-230.
6. I. Belharouak, W. Lu, J. Liu, D. Vissers and K. Amine, *J. Power Sources*, 2007, 174, 905-909.
7. K.-W. Nam, S.-M. Bak, E. Hu, X. Yu, Y. Zhou, X. Wang, L. Wu, Y. Zhu, K.-Y. Chung and X.-Q. Yang, *Adv. Funct. Mater.*, 2013, 23, 1047-1063.
8. S. Choi and A. Manthiram, *J. Electrochem. Soc.*, 2002, 149, A1157-A1163.
9. R. V. Chebiam, F. Prado and A. Manthiram, *J. Electrochem. Soc.*, 2001, 148, A49-A53.
10. K. Shizuka, C. Kiyohara, K. Shima, K. Okahara, K. Okamoto and Y. Takeda, *ECS Transactions*, 2008, 11, 7-13.
11. S. N. Lim, W. Ahn, S.-H. Yeon and S. B. Park, *Electrochim. Acta*, 2014, 136, 1-9.
12. D.-J. Lee, B. Scrosati and Y.-K. Sun, *J. Power Sources*, 2011, 196, 7742-7746.

13. Y. Cho, Y.-S. Lee, S.-A. Park, Y. Lee and J. Cho, *Electrochim. Acta*, 2010, 56, 333-339.
14. Y. Cho and J. Cho, *J. Electrochem. Soc.*, 2010, 157, A625-A629.
15. J.-H. Ju, Y.-M. Chung, Y.-R. Bak, M.-J. Hwang and K.-S. Ryu, *Surf. Rev. Lett.*, 2010, 17, 51-58.
16. J. Eom, K. Sun Ryu and J. Cho, *J. Electrochem. Soc.*, 2008, 155, A228-A233.
17. H. B. Kim, B. C. Park, S. T. Myung, K. Amine, J. Prakash and Y. K. Sun, *J. Power Sources*, 2008, 179, 347-350.
18. Y. Kim and J. Cho, *J. Electrochem. Soc.*, 2007, 154, A495-A499.
19. K. Du, J. Huang, Y. Cao, Z. Peng and G. Hu, *J. Alloys Compd.*, 2013, 574, 377-382.
20. J.-H. Ju and K.-S. Ryu, *J. Alloys Compd.*, 2011, 509, 7985-7992.
21. K. Tasaki, A. Goldberg, J.-J. Lian, M. Walker, A. Timmons and S. J. Harris, *J. Electrochem. Soc.*, 2009, 156, A1019-A1027.
22. Y. S. Jung, A. S. Cavanagh, A. C. Dillon, M. D. Groner, S. M. George and S.-H. Lee, *J. Electrochem. Soc.*, 2010, 157, A75-A81.
23. Y. Kim, *J. Mater. Sci.*, 2013, 48, 8547-8551.
24. H. Liu, Y. Yang and J. Zhang, *J. Power Sources*, 2007, 173, 556-561.
25. H. Liu, Y. Yang and J. Zhang, *J. Power Sources*, 2006, 162, 644-650.
26. Y. S. Jung, P. Lu, A. S. Cavanagh, C. Ban, G.-H. Kim, S.-H. Lee, S. M. George, S. J. Harris and A. C. Dillon, *Adv. Energy Mater.*, 2013, 3, 213-219.
27. M. Yoshio, R. J. Brodd and A. Kozawa, *Science and Technologies Springer*, 2009.
28. B. Huang, X. Li, Z. Wang, H. Guo, L. Shen and J. Wang, *J. Power Sources*, 2014, 252, 200-207.
29. S. N. Lim, W. Ahn, S.-H. Yeon and S. B. Park, *Electrochim. Acta*, 2014, 136, 1-9.
30. W. Liu, G. Hu, K. Du, Z. Peng and Y. Cao, *Surf. Coat. Technol.*, 2013, 216, 267-272.
31. D.-J. Lee, B. Scrosati and Y.-K. Sun, *J. Power Sources*, 2011, 196, 7742-7746.
32. H. B. Kim, B. C. Park, S. T. Myung, K. Amine, J. Prakash and Y. K. Sun, *J. Power Sources*, 2008, 179, 347-350.
33. Y. Cho and J. Cho, *J. Electrochem. Soc.*, 2010, 157, A625-A629.
34. Y. Cho, Y.-S. Lee, S.-A. Park, Y. Lee and J. Cho, *Electrochim. Acta*, 2010, 56, 333-339.
35. J. Cho, *J. Mater. Chem.*, 2008, 18, 2257-2261.
36. J.-W. Lee, S.-M. Park and H.-J. Kim, *J. Power Sources*, 2009, 188, 583-587.
37. X. Pu and C. Yu, *Nanoscale*, 2012, 4, 6743-6747.
38. M.-H. Park, M. Noh, S. Lee, M. Ko, S. Chae, S. Sim, S. Choi, H. Kim, H. Nam, S. Park and J. Cho, *Nano Lett.*, 2014, DOI: 10.1021/nl501597s.
39. X. Xiong, Z. Wang, G. Yan, H. Guo and X. Li, *J. Power Sources*, 2014, 245, 183-193.
40. X. Xiong, Z. Wang, H. Guo, Q. Zhang and X. Li, *J. Mater. Chem. A*, 2013, 1, 1284-1288.
41. M. Noh and J. Cho, *J. Electrochem. Soc.*, 2013, 160, A105-A111.
42. J. Kim, Y. Hong, K. S. Ryu, M. G. Kim and J. Cho, *Electrochem. Solid-State Lett.*, 2006, 9, A19-A23.
43. Y. Cho, P. Oh and J. Cho, *Nano Lett.*, 2013, 13, 1145-1152.
44. M.-J. Lee, S. Lee, P. Oh, Y. Kim and J. Cho, *Nano Lett.*, 2014, 14, 993-999.
45. A. Boulineau, L. Simonin, J.-F. Colin, C. Bourbon and S. Patoux, *Nano Lett.*, 2013, 13, 3857-3863.
46. J. Lee, A. Urban, X. Li, D. Su, G. Hautier and G. Ceder, *Science*, 2014, 343, 519-522.
47. N. P. W. Pieczonka, Z. Liu, P. Lu, K. L. Olson, J. Moote, B. R. Powell and J.-H. Kim, *J. Phys. Chem. C*, 2013, 117, 15947-15957.
48. J. Cho and M. M. Thackeray, *J. Electrochem. Soc.*, 1999, 146, 3577-3581.
49. H. Lee and Y. M. Lee, *J. Korean Electrochem. Soc.*, 2012, 15, 115-123.
50. S.-T. Myung, K.-S. Lee, C. S. Yoon, Y.-K. Sun, K. Amine and H. Yashiro, *J. Phys. Chem. C*, 2010, 114, 4710-4718.



TOC figure

Nano-scale surface protecting layer of $\text{LiNi}_{0.8}\text{Co}_{0.15}\text{Al}_{0.05}\text{O}_2$ consisting of substituted V^{4+} ions in 3b sites leads to structural robustness under the most challenging test conditions.

(80 mm X 36 mm)